Journal of Catalysis **192,** 185–196 (2000)
doi:10.1006/jcat.2000.2838, available online at http://www.idealibrary.com on IDEAL®

Size Effects in Gas-Phase Photo-oxidation of Trichloroethylene Using Nanometer-Sized TiO_2 Catalysts

A. J. Maira, K. L. Yeung,[1] C. Y. Lee, P. L. Yue, and C. K. Chan

Department of Chemical Engineering, The Hong Kong University of Science and Technology, Clear Water Bay, Kowloon, Hong Kong

Received October 7, 1999; revised February 1, 2000; accepted February 4, 2000

TiO_2 catalysts were prepared by using a modified sol–gel technique and were characterized by X-ray diffraction (XRD), transmission electron microscopy (TEM), and N_2 physi-adsorption methods. The effects of different synthesis parameters on the size and morphology of' the TiO_2 particles were investigated. A method for obtaining TiO_2 with different primary and secondary particle sizes was developed. By changing the water concentration during the hydrolysis of titanium isopropoxide, amorphous titania gel spheres of well-defined morphology and particle size were prepared. These gel spheres define the secondary particle or aggregate size. Following controlled thermal and hydrothermal treatments the primary TiO_2 particles (anatase) were formed from the gel spheres without alteration of the aggregate size and shape. Anatase TiO_2 catalysts with crystal size of 2.3–30 nm and aggregate size of 100–900 nm were prepared for the gas-phase photo-oxidation of trichloroethylene (TCE). The catalyst performance for TCE degradation exhibited strong dependence on both primary and secondary particle sizes of TiO_2.

Key Words: **nanostructured catalyst; titanium dioxide; photocatalysis; volatile organic compounds; trichloroethylene; sol–gel method.**

INTRODUCTION

Volatile organic compounds (VOCs) are one of the most common indoor air pollutants (1). They are found not only in industrial and manufacturing sites but also in commercial workplaces and domestic households. Many of these compounds are not only irritants, but are also suspected carcinogens and pose a significant health risk (2). There is an urgent need to establish an effective method for VOC remediation from indoor air, since most modern buildings are designed with centralized air-handling systems where the bulk of the indoor air is recycled and recirculated through the building.

The traditional treatment methods for air-borne VOCs include incineration (i.e., thermal and catalytic combustion), adsorption, absorption, condensation, and biofiltration (1). Although absorption and adsorption columns are simple to operate and can have a large capacity for VOC removal, they respectively produce secondary liquid and solid wastes. Condensation and biofiltration methods have low efficiencies, while the capital investment and operating cost for incineration are high. The corrosive products from the degradation of halogenated compounds also pose a problem for both thermal and catalytic incineration.

Gas-phase photocatalytic oxidation is an attractive technology for the degradation of VOCs (3). It is economical and simple and can be easily implemented. Photocatalytic oxidation is effective in destroying a wide range of common organic pollutants (4–6). Simple organic compounds are readily mineralized to carbon dioxide and water at ambient conditions using molecular oxygen as the primary oxidant (7–10). However, complex molecules are more difficult to degrade and undesirable intermediates and by-products can be formed (11–14). In addition, the rate of decomposition may also be slow. Better catalyst design and formulation are necessary in order to improve its performance for pollution abatement.

Titanium dioxide is the commonly used environmental photocatalyst for the oxidation of gaseous or aqueous organic pollutants. The TiO_2 catalyst exhibits good activity for photo-oxidation of organic compounds when either oxygen or liquid oxidants are used (e.g., hydrogen peroxide or organoperoxides) (15, 16). It is also chemically stable, commercially available, and inexpensive. The photocatalytic oxidation occurs in the presence of a semiconductor catalyst (i.e., TiO_2) and UV or near-UV light source. The incident photons possessing energies greater than the band gap of the catalyst are absorbed. The absorbed photon then excites a valence electron into the conduction band, creating a positive hole. The resulting electron–hole pair can migrate toward the catalyst surface and initiate redox reactions that oxidize the adsorbed organic molecules.

A good photocatalyst must possess a large catalytic surface and should also exhibit a high photon utilization efficiency. The size of the primary catalyst particles defines the surface area available for adsorption and decomposition of the organic pollutants. When the size of a semiconductor

[1] To whom correspondence should be addressed. Fax: 852-2358-0054. E-mail: kekyeung@ust.hk.

0021-9517/00 $35.00

particle is decreased to the extent that the relative proportions of the surface and bulk regions of the particle are comparable, its energy band structure becomes discrete and will exhibit chemical and optical properties different from those of the bulk material (17). This is known as the quantum size effect and has been observed for nanometer-sized TiO_2 particles (18). Aggregation of the TiO_2 primary particles is difficult to avoid. The morphology and size of these aggregates or secondary particles can affect the light-scattering properties of the catalyst (19, 20), as well as the degree of photon penetration. The transport properties of the reactants and products within the aggregate can also alter the effectiveness of the catalyst.

The relationship between the particle size and photocatalytic activity of TiO_2 has been addressed (21–25). Anpo *et al.* (21) observed an increase in the TiO_2 photocatalytic activity for the hydrogenation of CH_3CCH with decreasing particle size. They associated the pronounced activity enhancement for particles smaller than 10 nm with the combined effects of larger surface area and size quantization. A similar observation was also made for the photocatalytic degradation of methylene blue in aqueous suspension for a series of TiO_2 particles larger than 30 nm (22). However, other reports showed that the photocatalytic efficiency does not monotonically increase with decreasing particle size (23–25). An optimal particle size of about 10 nm was observed for nanocrystalline TiO_2 photocatalysts in the liquid-phase decomposition of chloroform (23, 24). This phenomenon was attributed to the increased surface e^-/h^+ recombination rate, which offsets the benefits of ultrahigh surface area (24). Indeed, Rivera *et al.* (25) had reported a linear increase in photocatalytic oxidation of trichloroethylene with increasing anatase crystal size. The significant disagreements in the effects of particle size on the photocatalytic activity of TiO_2 warrant a careful study.

This paper addresses the preparation, characterization, and catalytic activity of nanometer-sized anatase TiO_2 particles. Titanium dioxide photocatalysts of exact particle sizes (i.e., primary particles) and crystalline phase were prepared using a modified sol–gel method. The technique also provides precise control over the size and morphology of the aggregates (i.e., secondary particles). A systematic study of the synthesis parameters was conducted to determine their effect on the structural and chemical properties of the TiO_2 photocatalysts. Finally, the activity of the catalysts was determined for gas-phase photo-oxidation of trichloroethylene.

EXPERIMENTAL

Synthesis of Nanometer-Sized TiO_2 Particles

There have been many reports of titanium dioxide photocatalysts being successfully prepared using inorganic (e.g., $TiCl_4$) and organometallic (e.g., titanium alkoxide) precursors in the gas phase or the liquid phase (26–32). The sol–gel process is an attractive method for low-temperature synthesis of nanostructured TiO_2 particles. The synthesis procedures are simple and convenient, resulting in high-purity products (33, 34). During the sol–gel synthesis, the titanium alkoxides undergo hydrolysis, polymerization, and condensation reactions that determine the size and structure of the final TiO_2 particles. Previous studies (30, 35–37) indicated that water concentration was a critical factor in determining the TiO_2 particle size. The preparation of nanometer-sized TiO_2 particles is, however, quite difficult. Special synthesis procedures, such as confining the hydrolysis reaction within the micellar volume and using a stearic stabilizer, were necessary for preparing particles smaller than 10 nm (38).

In commercial processes, the TiO_2 particles are prepared by a hydrocarbon-assisted flame synthesis (39). The synthesis methodology dictates the morphology and size of the resulting catalyst particles. Figure 1 shows the microstructures of TiO_2 catalysts prepared by flame pyrolysis (commercial Degussa P25) and sol–gel methods. The P25 TiO_2 is a complex oxide with coexisting anatase and rutile phases. It consists of 25–30-nm primary particles forming a loose aggregation measuring 140–170 nm (cf. Fig. 1a). Figure 1b displays the microstructure of a TiO_2 powder prepared by the sol–gel technique. The particles have uniform particle size (11 nm) and are pure anatase.

In this study, a modified sol–gel method was employed to obtain TiO_2 photocatalysts of controlled crystal and aggregate sizes. The synthesis conditions were adjusted to yield identical aggregate morphology. For this study, the aggregate shape was spherical. After titanium isopropoxide (TIP, Aldrich) was chosen as the main precursor, the synthesis was conducted in a dry, nitrogen environment. The precursors were mixed with an alcohol–water solution at a constant temperature. A specially designed apparatus was employed to regulate the addition of the alkoxides. The effects of the titanium isopropoxide and water concentration, $[H_2O]/[TIP]$ ratio, TIP addition rate, and mixing rate were investigated. Table 1 summarizes the range of conditions employed in the sol–gel synthesis.

Following the sol–gel preparation, controlled thermal and/or hydrothermal treatments were used to transform

TABLE 1

Range of Conditions Employed in the Modified Sol–Gel Synthesis

Parameter	Range	Effect on amorphous particle size
TIP concentration	0.1–3 mM	No
H_2O concentration	1–20 M	Yes
$[H_2O]/[TIP]$ ratio	4–300	No
TIP addition rate	0.06–3 cm^3/min	No

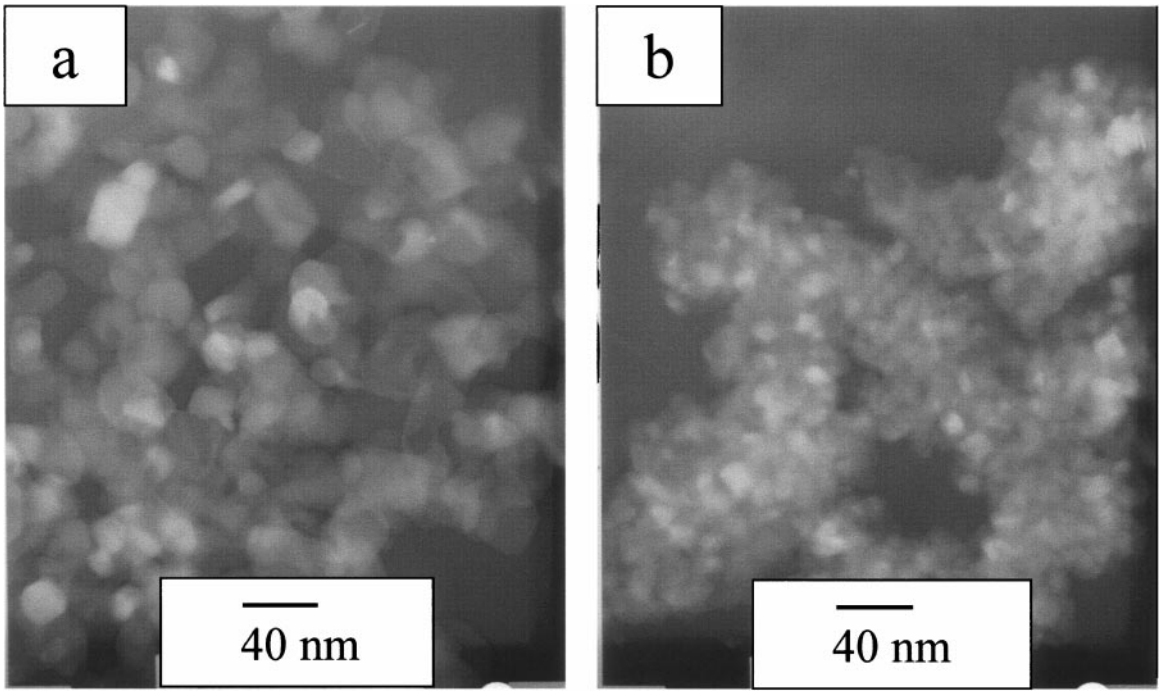

FIG. 1. Microstructure of (a) commercial Degussa P25 TiO_2 and (b) TiO_2 prepared by the sol–gel method.

the amorphous titania into crystalline anatase. For the thermal treatment, the amorphous titania powder was heated in a high-temperature furnace and calcined in flowing air. The anatase TiO_2 powder was then stored in a sealed bottle for subsequent analysis and use. The hydrothermal treatment was conducted in a 150-ml, Teflon-line autoclave vessel (PTFE-4748, Parr Scientific). The amorphous powder (~0.2 g) was mixed with an alcohol–water solution and transferred into the autoclave vessel. The vessel was then heated in a preheated, air-convection oven (Memmert, UE200-220C-SS). The resulting anatase TiO_2 powder was recovered by centrifugation and rinsed with deionized distilled water. The powder was dried in an oven at 338 K for 24 h before it was placed in a storage bottle.

Characterization of Nanometer-Sized TiO_2 Particles

The crystal structure, particle size, morphology, and surface area of the TiO_2 photocatalysts were characterized using X-ray diffraction (XRD), transmission electron microscopy (TEM), and N_2 physi-adsorption. The dried sample powder was analyzed by XRD using a Philips PW 1030 X-ray diffractometer with a Cu$K\alpha$ radiation source and a graphite monochromator. The patterns were recorded for $23 < 2\theta < 60$ at a scan rate of 0.05 s^{-1}. The phase structure, crystallinity, and grain size of the TiO_2 particles were determined from the X-ray diffraction patterns.

For TEM imaging, the sample powder was dispersed in isopropanol and a drop of the suspension was placed onto a carbon-coated copper grid. The excess liquid was removed using a paper wick and the deposit was dried in air prior to imaging. The deposited TiO_2 particles were examined with a Philips CM20 transmission electron microscope at an accelerating voltage of 200 kV. Only the energy signatures corresponding to the Ti and O elements were obtained from the *in situ* analysis of the particles with energy dispersive X-ray spectroscopy (EDXS, Philips XL30). The size and morphology of the primary and secondary TiO_2 particles were measured from the TEM micrographs. The BET surface area of the TiO_2 photocatalyst was measured using the N_2 physi-adsorption technique (Micromeritics ASAP 2010). The dried powder was outgassed under vacuum at 523 K for 4 h prior to the analysis.

The surface composition of the catalyst samples was determined by X-ray photoelectron spectroscopy (XPS, Physical Electronics PHI 5600) using a monochromatic aluminum X-ray source. The catalyst powder was pressed onto a double-sided carbon tape to make a flat surface and then introduced into the instrument for analysis. The Raman spectra were measured using a Renishaw 3000 micro-Raman system with an Olympus BH-2 microscope. The objective lenses with $20\times$ and $50\times$ magnifications were selected. The excitation source used was an argon laser operating at 514.5 nm with an output power of 25 mW. Raman spectra were taken of the powders on a glass microscope slide. The spectral resolution was set at approximately 1.0 cm^{-1} and the spot size was about 2 μm in diameter. The absorption spectra of the TiO_2 catalysts were measured using a Philips/Unicam Pu8700 UV/vis spectrometer with

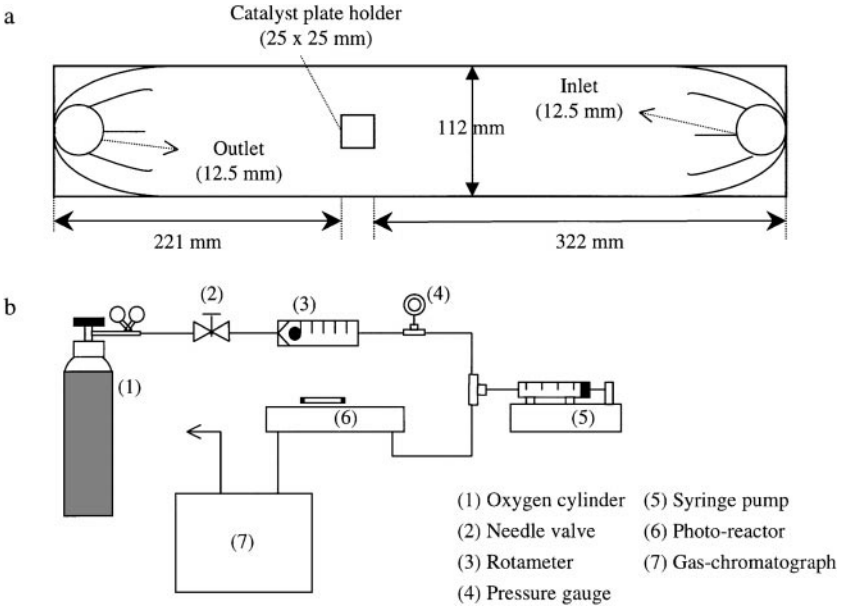

FIG. 2. Schematic diagrams of (a) the photoreactor and (b) the experimental set-up.

diffuse and specular reflection accessories. A Ba_2SO_4 standard white plate was used as background. The spectra were recorded at a scan speed of 125 nm/min and a bandwidth of 2 nm. For the analysis, the TiO_2 powders were diluted with NaCl (5 wt% TiO_2).

Evaluation of Nanometer-Sized TiO_2 Particles

Figure 2 shows the schematic diagrams of the photoreactor unit and experimental set-up used for evaluating the performance of TiO_2 catalysts for the gas-phase photo-oxidation of trichloroethylene. The flat, rectangular photoreactor had dimensions of 578 mm $\times$ 113 mm. The stainless steel reactor contained the inlet and outlet ports, a recess for the catalyst plate, and two sets of machined baffles (cf. Fig. 2a). A 6.25-mm-thick Pyrex glass cover completes the reactor assembly. The Pyrex glass window and the stainless steel reactor form a narrow rectangular channel (2 mm deep $\times$ 112 mm wide) for gas flow. The gases enter normal to the reactor channel and flow through the baffles. The baffles were designed to help distribute the gases uniformly along the width of the channel. The flow was allowed to develop before reaching the catalyst bed 322 mm downstream from the entrance. The gases were then guided by the next set of baffles to the reactor exit.

The catalyst plate was prepared by coating a thin layer of TiO_2 catalysts on a flat support. A porous stainless steel (SS-316L) plate from Mott Metallurgical was selected for the support material. The SS-316L plate had a nominal pore size of 0.2 μm and had a thickness of 1 mm. It measured 25 mm^2 and had an area of 6.3 cm^2. The support was cleaned by a sequence of sonication in trichloroethylene (Fisher) and ethanol (RDH) solutions in order to remove dirt and contaminants. After the support was dried in an oven at 373 K overnight, one side of the support was coated with a layer of TiO_2 catalyst.

To obtain a uniform catalyst layer, the support was first pretreated with a surfactant, mercaptopropyltrimethoxysilane (MPS, Aldrich, 95%). The support was immersed in 4.2 mM MPS–ethanol solution for 30 min. This procedure attaches the mercapto end of MPS molecules to the support material, while exposing the silanol head groups. The plate was then slip-cast with 0.6 M suspension of TiO_2 particles in isopropanol for 1 min and dried in air. After drying of the plate at 473 K for 3 h, the silanol condenses, providing a strong anchoring for the TiO_2 particles. Thick layers of catalyst can be prepared using this method without crack formation or film delamination.

The experimental equipment shown in Fig. 2b consists of the gas and vapor feed delivery module, the reactor, and the analytical instrument. The liquid TCE feed was delivered to a constant-temperature heat exchanger using a syringe pump (kdScientific 1000). The vaporized TCE was mixed with flowing oxygen (HP, HKO) before entering the photoreactor. The flow rate of dry oxygen was adjusted using a calibrated flow meter. The reactant mixture then entered the reactor and flowed over the catalyst plate. The photocatalyst was illuminated by five fluorescent black lamps (6 W, BLB Sankio Denki) located 7 mm above the reactor window. The outlet gases were separated using a GS-GASPRO capillary column (0.32 mm $\times$ 30 m) and analyzed using a gas chromatograph (HP 6890) equipped with thermal conductivity and flame ionization detectors. The gases used in the GC were helium (UHP, CW), hydrogen (UHP, HKO), and synthetic air (HP, HKSP). An on-line gas analyzer (Bruel & Kjaer, Type 1302) also provided transient data

for the reaction and was useful in determining the steady state.

The performance of the anatase-phase TiO_2 catalysts was studied for the gas-phase photo-oxidation of trichloroethylene. The reaction was carried out at ambient temperature and pressure. In a typical experiment, a catalyst plate coated with 6 mg of TiO_2 was placed in the reactor. The flow rate of oxygen entering the reactor was maintained at 100 sccm with the concentration of TCE fixed at 0.01 mM (i.e., 240 ppm). After the reaction reached steady state, the composition of the outlet was analyzed to provide the initial TCE concentration, $[TCE]_i$. The UV lamps were switched on and the reactor effluent was monitored until a constant TCE concentration (i.e., $[TCE]_f$) was obtained. The steady-state TCE consumption rate can then be calculated from the initial and final TCE concentrations.

RESULTS AND DISCUSSION

Synthesis and Characterization of Nanometer-Sized TiO_2

Amorphous titania gel spheres. The modified sol–gel method provides a means for the preparation of amorphous titania gel spheres of well-defined morphology and size. Although particles of different shapes (e.g., plates and fibers) can be prepared, it was decided that a spherical shape was more suitable for the purpose of this study. Figure 3 shows the effects of precursor and water concentrations on the size of the amorphous titania particles. The titanium precursor was added drop by drop to the alcohol–water solution, and the [TIP] shown in Fig. 3a refers to its final concentration after the last drop of TIP was added. Figure 3a indicates that the particle size is independent of the concentration of the TIP precursor.

Figure 3b plots the particle size of the amorphous titania as a function of the water concentration at a fixed TIP addition rate of 0.2 ml/min and a $[H_2O]/[TIP]$ ratio of 4. The particle size decreases rapidly with water addition, reaching a constant value at high water concentration. This behavior can be explained if we consider that the increase in water content of the synthesis mixture results in a higher homogeneous nucleation rate (34) and therefore smaller gel spheres. At a constant $[H_2O]/[TIP]$ ratio, increasing the water concentration also means a smaller reaction volume and higher [TIP] concentration. At $[H_2O] > 0.5$ M, a critical value was reached and particle sizes smaller than 80 nm could not be obtained.

TABLE 2

XPS Data of the Surface Composition of Amorphous Titania Gel and Anatase TiO_2 Particles

Crystalline phase	Primary particle (nm)	Secondary particle (nm)	C (%)	O (%)	Ti (%)
Amorphous	—	100	34	47	19
Anatase	11	100	21	55	24
Anatase	11	600	21	55	24

Figure 4 displays the transmission electron micrographs of amorphous titania particles prepared at water concentrations of 2.3, 0.3, 0.27, and 0.18 M. It is clear from the images that the size of the titania decreases with increasing water content of the synthesis mixture. All of the titania particles have a similar spherical shape. No crystalline phases or grain structure can be detected on the particles even at high magnification. The images in Fig. 4 also show that the titania particles were agglomerated. However, this may be an artifact of the TEM sample preparation rather than a true reflection of the state of agglomeration of the particles. Table 2 gives the data on the surface composition of the amorphous titania obtained by XPS analysis. The results show that the main components are titanium and oxygen which is similar to that obtained by *in situ* EDXS. Carbon was present mostly in the form of adsorbed atmospheric contaminants (e.g., CO_2 and hydrocarbons) but the presence of ethanol and unreacted ethoxide cannot be ruled out.

Figure 5a shows that changing the $[H_2O]/[TIP]$ ratios does not affect the size of the amorphous titania particles.

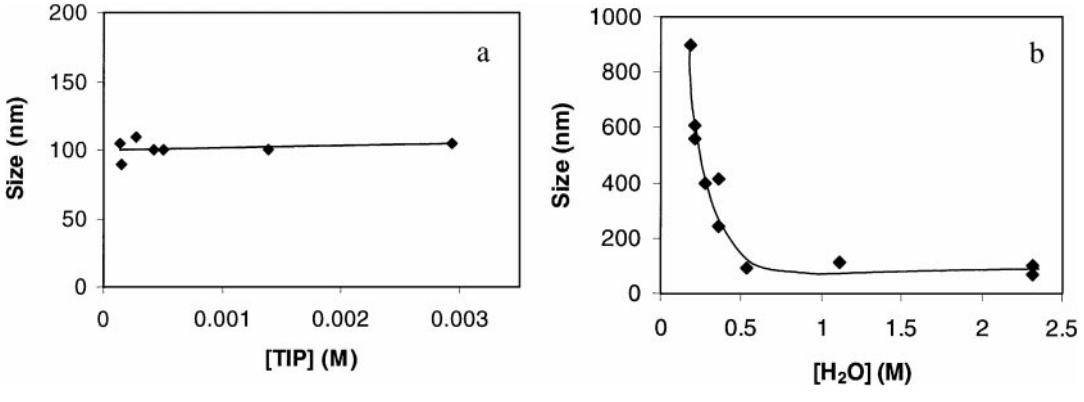

FIG. 3. Effects of (a) titanium isopropoxide (TIP) and (b) water concentrations on the size of the amorphous titania gel particles.

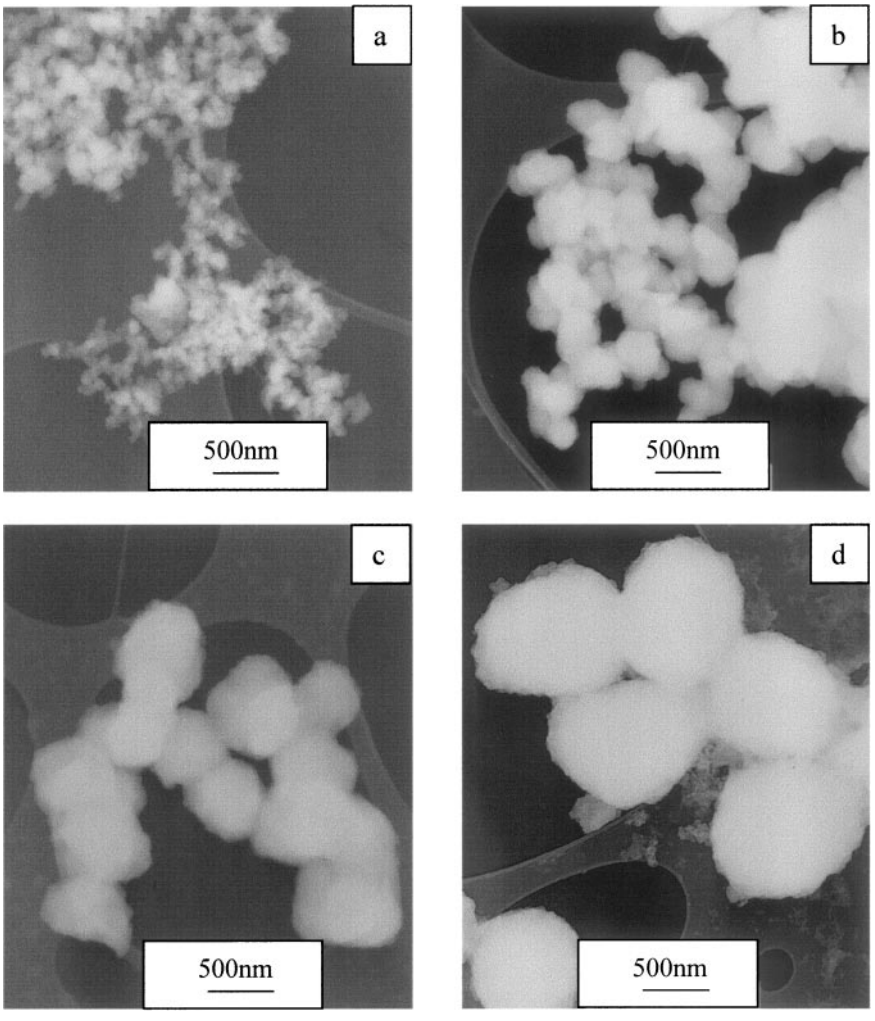

FIG. 4. Transmission electron microscopy images of amorphous titania gel particles prepared at water concentrations of (a) 2.3, (b) 0.3, (c) 0.27, and (d) 0.18 M.

In these experiments, the quantity of TIP was fixed and the amount of water was varied while the concentration of water in the alcohol solution was maintained as a constant. The ratio $[H_2O]/[TIP]$ has been reported to affect the hydrolysis process at a nonstoichiometric value (35). However, in that case the alkoxide hydrolysis is incomplete and the obtained powder contains a significant amount of organic residue (35).

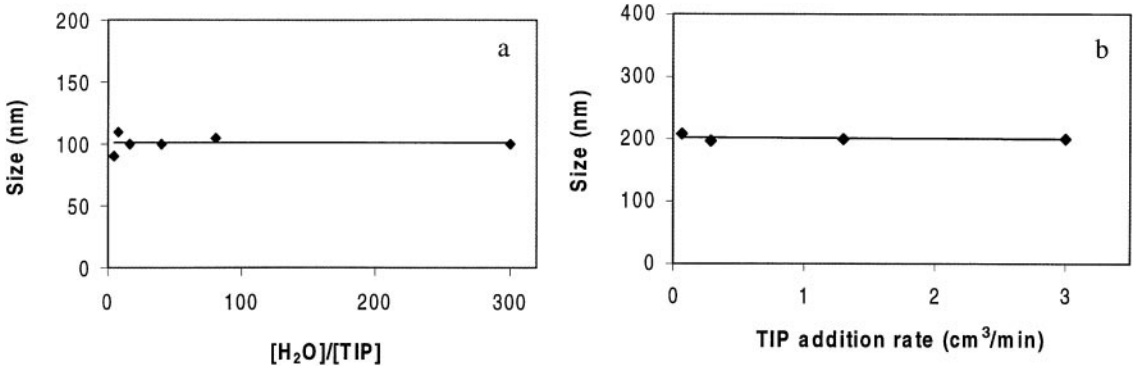

FIG. 5. Effects of (a) $[H_2O]/[TIP]$ ratio and (b) TIP addition rate on the size of the amorphous titania gel particles.

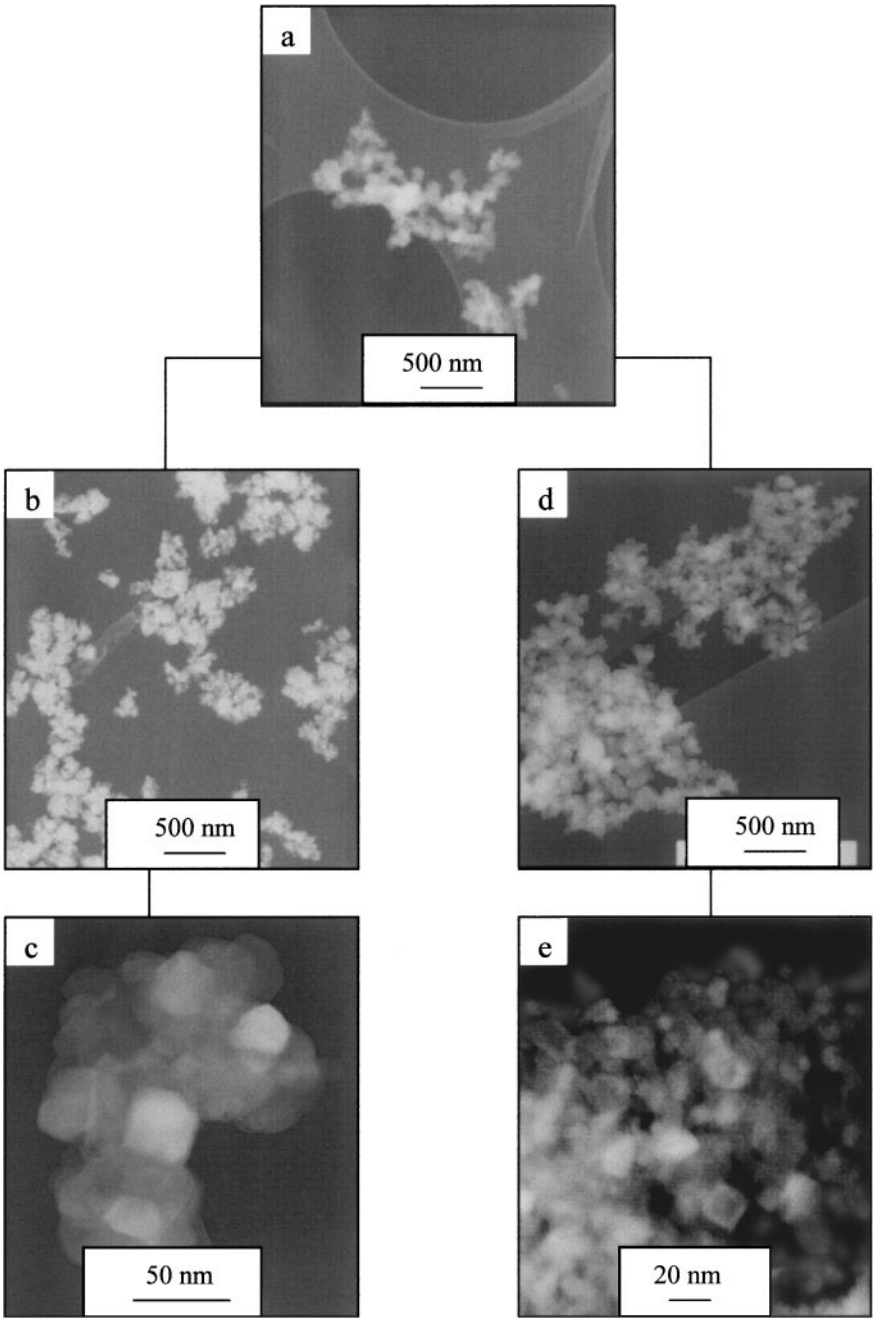

FIG. 6. Transformation of (a) amorphous titania gel particles into crystalline anatase–TiO_2 using (b,c) thermal and (d,e) hydrothermal processes.

The size of the titania particles (Fig. 5b) is also independent of the addition rate of TIP at constant [TIP] and [H_2O] of 8.9×10^{-5} and 0.36 M, respectively. The titanium isopropoxide was added drop by drop into the alcohol–water solution to ensure complete hydrolysis of the titanium alkoxide. This result indicates that the rate of hydrolysis under a well-mixed condition was rapid. Although the mixing rate does not have a pronounced effect on the particle size, it was observed that the particles prepared from stagnant solutions exhibit irregular morphology and broad particle size distribution. These effects can be attributed to the low miscibility between the metal alkoxide and the alcohol–water solution that led to a higher local concentration of TIP precursor and depletion of surrounding water reactant. This resulted in uneven nucleation of the titania from the solution.

Crystalline anatase–TiO_2. The amorphous titania (Fig. 6a) was transformed into crystalline TiO_2 particles using thermal (Figs. 6b and 6c) and hydrothermal processes

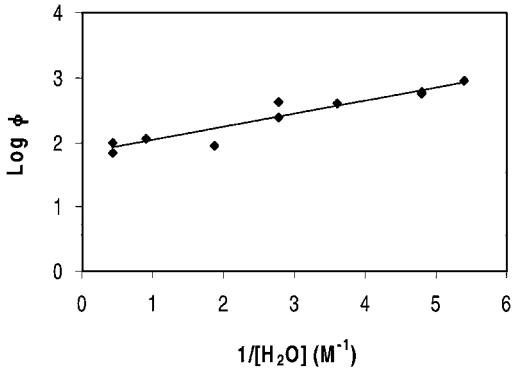

FIG. 7. Empirical correlation between the secondary particle size (ϕ) and the initial water concentration in the modified sol–gel synthesis mixture.

(Figs. 6d and 6e). The figures show that the crystalline phase was nucleated and formed from the amorphous titania material (Figs. 6c and 6e). The genesis transformed the amorphous titania sphere into an aggregate of TiO_2 crystals. The shape and size of the aggregate or secondary particle (Figs. 6b and 6d) were identical to those of the original amorphous titania (Fig. 6a). Indeed, a good correlation can be obtained between the secondary particle size and the initial water concentration in the sol–gel synthesis mixture as shown in Fig. 7. This relationship can be expressed by a simple empirical equation,

$$\mathrm{Log}\,\phi(\mathrm{nm}) = 1.748 + 0.218/[\mathrm{H_2O}],$$

where ϕ is the TiO_2 secondary particle size in nanometers, and $[H_2O]$ is the molar water concentration.

Thermal treatment usually led to coarser TiO_2 crystals, while hydrothermal treatment yielded finer crystal size as shown in Figs. 6c and 6e. It is evident from the TEM micrographs that these TiO_2 crystals or primary particles were aggregated into spherical ensembles with a porous and open structure. In both samples, sharp electron diffraction patterns corresponding to those of crystalline solids were obtained from the nanometer-sized crystals. X-ray diffraction analyses of the particles shown in Figs. 6c and 6e reveal pure anatase TiO_2 crystal structure. Only titanium and oxygen were detected by *in situ* EDXS analysis of the primary particles. The XPS measurements also gave similar results for the surface composition of the crystalline samples, with adsorbed atmospheric carbons being the main surface contaminant (Table 2). The modified sol–gel method combined with thermal and hydrothermal treatment process enabled the synthesis of anatase TiO_2 photocatalysts with primary particle size between 2.3 to 30 nm and secondary particle size ranging from 100 to 900 nm.

During the thermal treatment of the amorphous titania condensation and polymerization reactions will continue, expelling water molecules and producing a denser structure. This eventually led to crystallization and growth of anatase crystals, and their final transformation into a rutile crystal structure (40). Figure 8 shows the results of the thermogravimetric (TGA) and differential thermal analyses (DTA) performed on two amorphous titania samples with particle sizes of 100 and 900 nm. The experiments were conducted in flowing air at a heating rate of 10 K/min from 298 to 1173 K. Most of the weight loss occurred at around 373 K and was accompanied by heat absorption as indicated by the endothermic peak in the DTA plot (Fig. 8b). This can be attributed to sample dehydration during the heat treatment. After the initial weight loss, the weight of the titania sample remains constant up to the final temperature of 1173 K (Fig. 8a). A small exothermic peak was observed at 723 K coinciding with the formation of crystalline anatase-phase.

Thermal treatment is a common method used for obtaining crystalline TiO_2 (40). It is simple as well as convenient, and lends itself well to controlling the crystal size. However, great care must be exercised in order to ensure reproducibility. Another drawback of the thermal technique is the difficulty in obtaining pure anatase TiO_2. The crystalline anatase TiO_2 is formed only at temperatures above 723 K. Table 3 summarizes some of the particle sizes obtained using heat treatment. The temperature and time dictate the crystal size of the primary particles. Higher temperatures resulted in particle sintering and larger primary particles. The largest pure anatase TiO_2 crystal size obtained by heat treatment was 35 nm. By following a careful heat treatment procedure, crystals larger than 35 nm containing less than

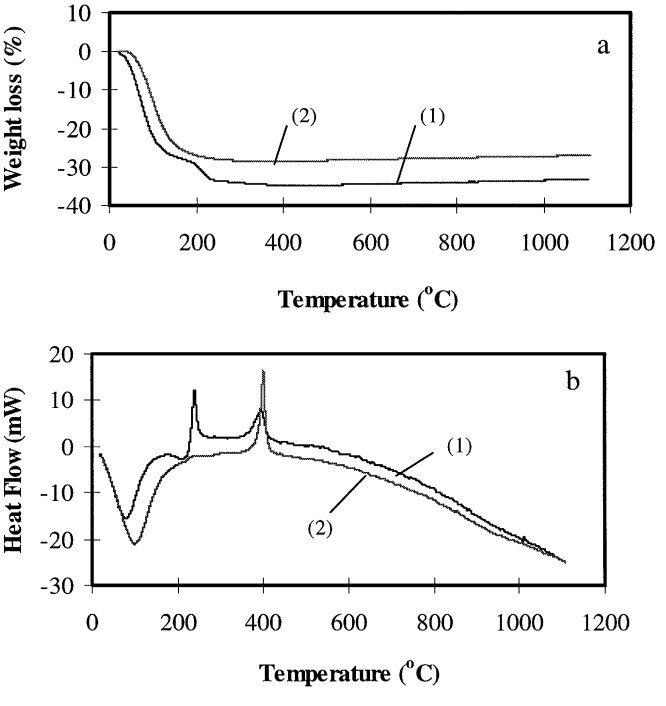

FIG. 8. (a) Thermogravimetric (TGA) and (b) differential thermal analyses of the crystallization of anatase TiO_2 from the amorphous titania gel particles of (1) 100 nm and (2) 600 nm sizes.

TABLE 3

Conditions Used in the Thermal and Hydrothermal Treatments

Sample	Particle size		Preparation conditions
	Primary[a]	Secondary[b]	
P02S100	2.3 nm	100 nm	17 ml of H_2O + 8 ml of isopropanol, 100°C for 8 h
P04S100	3.8 nm	100 nm	15 ml of H_2O + 10 ml of isopropanol, 100°C for 8 h
P05S100	5.2 nm	100 nm	15 ml of H_2O + 10 ml of isopropanol, 150°C for 8 h
P07S100	7.0 nm	100 nm	10 ml of H_2O + 15 ml of isopropanol, 150°C for 8 h
P08S100	8.5 nm	100 nm	2.5 ml of H_2O + 25 ml of isopropanol, 150°C for 8 h
P11S100	11 nm	100 nm	Air, 450°C for 3 h
P27S100	27 nm	100 nm	Air, 700°C for 15 min

[a] Primary particle size measured from XRD line broadening.
[b] Secondary particle size determined by TEM analysis.

5% rutile phase were prepared. A 65-nm sample with more than 90% anatase crystal was also synthesized. Although similar work had been conducted on the preparation of rutile TiO_2, the discussion in this paper will be mainly on the anatase TiO_2 materials.

Hydrothermal treatment has been employed in the preparation of zeolites (41) and the crystallization of metal oxides (43, 44). In this study, hydrothermal treatment was used to prepare anatase TiO_2 crystals with primary particle sizes between 2.3 and 11 nm. The crystal size was controlled by the composition of the alcohol–water mixture used in the hydrothermal reaction. The reaction temperature and treatment time were used in fine-tuning the crystal size and for ensuring the crystallinity of the final product. Unlike thermal treatment, this method demonstrates good reproducibility and yields only pure anatase TiO_2. Table 3 shows the exact conditions used in the preparation of the anatase TiO_2 using hydrothermal treatment. The bulk and surface compositions of the primary particles were mainly Ti and O.

Although Fig. 6 shows that TEM imaging can clearly distinguish the primary particles from the aggregates (i.e., secondary particles), it was difficult to measure the *exact* size of the anatase TiO_2 crystals from the micrograph. Instead, XRD line broadening was used for determining the primary particle size. The results were usually in good agreement with the TEM data. Figure 9 displays the X-ray diffraction patterns of the anatase TiO_2 catalysts with different primary particle sizes. The anatase diffraction peaks are broader and have weaker intensity for smaller particle sizes as expected (44). The larger secondary particles were measured directly from the TEM micrograph.

Figure 10 plots the BET surface area of the anatase TiO_2 catalysts as a function of primary (Fig. 10a) and secondary (Fig. 10b) particle sizes. Figure 10a shows that the catalyst's surface area decreases with increasing primary particle size. At a fixed aggregate size of 100 nm, the smallest (2.3 nm) and the largest (25 nm) anatase TiO_2 crystals gave surface areas of 268 and 28 m^2/g, respectively. Figure 10b displays the BET surface area of samples with 11 nm primary particle size and different secondary particle sizes. The secondary particle size does not affect the surface area of

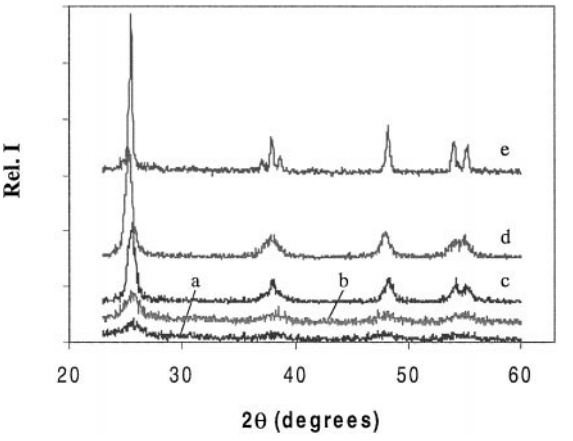

FIG. 9. X-ray diffraction patterns of anatase TiO_2 with primary particle sizes of (a) 2.3, (b) 3.8, (c) 7, (d) 11, and (e) 29 nm.

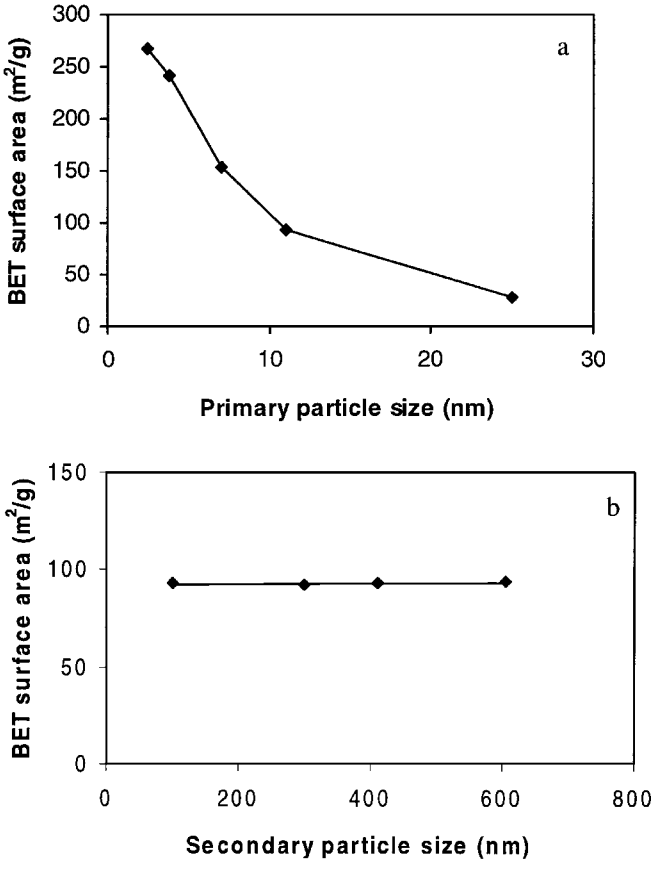

FIG. 10. BET surface area of anatase TiO_2 as a function of (a) primary particle size and (b) secondary particle size.

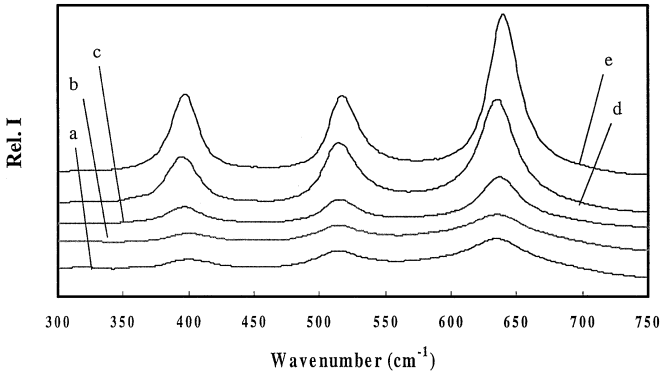

FIG. 11. Micro-Raman spectra of anatase TiO_2 with primary particle sizes of (a) 2.3, (b) 3.8, (c) 7, (d) 11, and (e) 29 nm.

the catalyst. These results suggest that the catalyst's surface area is dependent only on the size of anatase TiO_2 crystals and is unaffected by the size of the aggregate.

Raman spectroscopy has been used to characterize TiO_2 catalysts prepared by the sol–gel method (45–47). Raman spectroscopy wave vector selection rules, which limit the wave vector of detectable phonons to the Brillouin zone center, break down at a sufficiently small size (>10 nm). As a result, all the spectra peaks broadened with decreasing particle size (45). Figure 11 reports the Raman spectra of TiO_2 with different primary particle sizes. There was no significant shift in the spectral lines even for the smallest TiO_2 particles (2.3 nm). The peak intensity decreases and the spectral line broadens with decreasing particle size. A strong correlation between Raman line broadening and TiO_2 particle size has been reported (45). Iida and coworkers (45) claim that this method is more sensitive for nanometer-sized crystals than X-ray line broadening.

Photocatalytic Activity of Nanometer-Sized TiO_2

The catalytic activity of the nanometer-sized TiO_2 was investigated using gas-phase TCE photo-oxidation as a probe reaction. Figure 12a shows the TCE reaction rates for different primary particle sizes at a fixed aggregate size of 100 nm. The activity of the commercial Degussa P25 TiO_2 catalyst was also included for comparison. The prepared nanometer-sized TiO_2 has higher activity than the commercial catalyst (Fig. 12a). The figure shows an enhancement in the rate of TCE conversion as the TiO_2 crystal size decreases from 27 to 7 nm. However, the catalyst activity dropped when smaller TiO_2 primary particles (i.e., 3.8 and 2.3 nm) were used. The results suggest that an optimum TCE degradation can be obtained from catalyst with 7-nm TiO_2 crystals. A similar behavior had been reported for liquid-phase decomposition of $CHCl_3$ or TCM, where the best TCM conversion was obtained from 10-nm TiO_2 particles (24).

It is clear from Fig. 12a that the photocatalytic activity of the TiO_2 is strongly influenced by crystal size. As the size of TiO_2 diminishes, both the structural and electronic properties of the TiO_2 can undergo significant changes with important consequences on its catalytic activity. The smaller TiO_2 crystals have a larger surface area for the adsorption of reactants. This will make a positive contribution to the catalyst reactivity. For particles smaller than 11 nm, the surface structure of the atom ensembles can deviate from that of a bulk crystal. This could result in a significant difference in the number and types of catalytic sites present in nanocrystals and that of a larger crystal.

The small crystal size also gave rise to quantum size effects (17). This results in a net shift in the semiconductor band-gap to higher energies as shown by UV absorption spectra of TiO_2 catalysts in Fig. 13. A blue shift in the TiO_2 band gap occurred for crystals smaller than 11 nm. This means that for the same light source, there are fewer photons with the required energy to generate the e^-/h^+ pairs needed for the reaction. This results in a lower utilization of photons. The modified electronic band-gap structure of the TiO_2 could increase or decrease the photocatalytic activity depending on the reduction–oxidation potential of

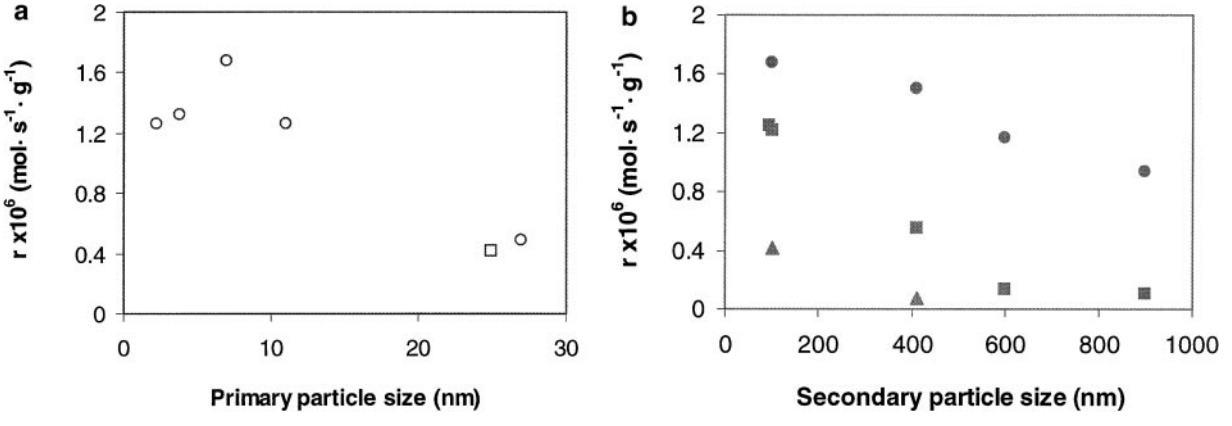

FIG. 12. (a) TCE conversion rate as a function of anatase TiO_2 primary particle size. [(○) TiO_2 prepared by the sol–gel process. (□) Commercial TiO_2 P25.] (b) TCE conversion rate as a function of anatase TiO_2 secondary particle size. [Primary particle sizes of (●) 7, (■) 11, and (▲) 25 nm.]

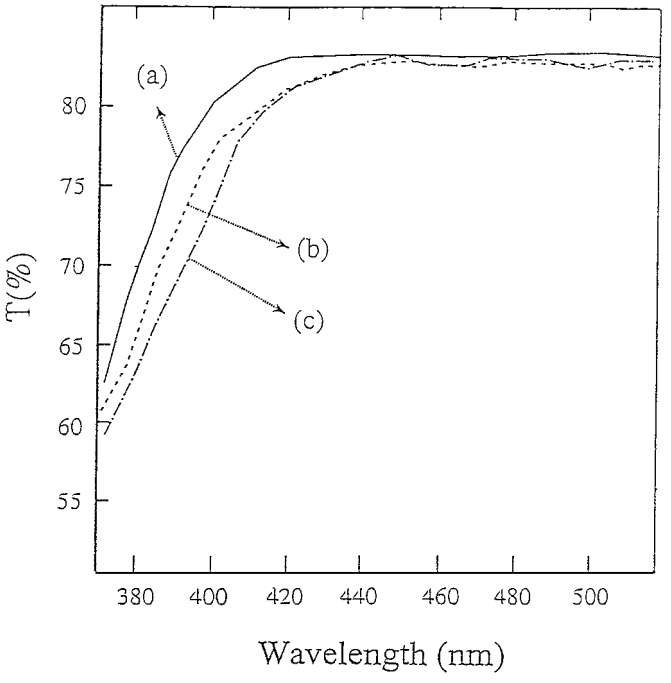

FIG. 13. UV absorption spectra of anatase TiO_2 with primary particle sizes of (a) 3.8, (b) 6, and (c) 11 nm.

the adsorbed organic compounds. For the photo-oxidation of TCE vapor, the reaction data indicate that surface area plays a dominant role for TiO_2 with primary particle size larger than 7 nm (Fig. 12a). It is, however, difficult to attribute the subsequent drop in reactivity wholly to either structural or electronic effects.

Figure 12b plots the TCE conversion rate as a function of secondary particle size for TiO_2 catalysts with primary crystal sizes of 7, 11, and 25 nm. It is evident that the secondary particle size has a strong effect on the catalytic activity of TiO_2 for TCE photo-oxidation. For aggregates smaller than 600 nm, the TCE conversion exhibits a rapid linear decline with increasing secondary particle size. If the lower reactivity of the TiO_2 catalysts with larger secondary particle sizes is due to the higher intercrystalline diffusional resistance across the aggregate, it is expected that the reactivity of the smaller TiO_2 crystals should exhibit a stronger dependence on the secondary particle size. However, Fig. 12b shows that the decline in the reactivity with the aggregate size is more pronounced for the larger TiO_2 crystals.

A more likely explanation is as follows. Unlike traditional gas-phase catalysis, the absorption of photons is needed to activate the TiO_2 catalyst for photoreaction. The quantity of photons reaching the core of a spherical aggregate depends on the size of the secondary particle and the optical properties of the TiO_2 crystals. The smaller crystals are generally poorer light scatterer than larger crystals, since the scattering efficiency is proportional to r^4 in Rayleigh scattering (48). Also, the penetration of light into the aggregate is influenced by the superficial morphology of the aggregates (47). Secondary particles formed from large TiO_2 crystals have smoother surfaces than the aggregates made from small crystals. On the smooth surface, the incident photons are scattered and lost mostly by reflection. The rougher surface formed by the nanocrystals allows a greater number of scattered photons to penetrate into the aggregate. Figure 12b shows that the decline in reactivity with the aggregate size is more pronounced for larger crystal size. This suggests that photon penetration into the aggregated TiO_2 crystals is a more likely explanation for the observed dependence of the photoreactivity on the secondary particle size.

Several studies (49–51) of the effects of TiO_2 crystalline phase structure on its photoreactivity indicated that the anatase phase is more active than the rutile phase. However, the transformation process from anatase to rutile is usually accompanied by a rapid growth in the crystal size (40, 50). Therefore, it is not certain if the higher activity of the anatase phase is due primarily to the crystalline structure and not the crystal size (i.e., primary particle size). In this work, a pair of 40-nm anatase and rutile TiO_2 catalysts was prepared with an aggregate size of 100 nm. The rutile TiO_2 catalyst had a surface area of about 3 m^2/g and was inactive for TCE photo-oxidation. The anatase TiO_2 with the same particle size also exhibited low reactivity for TCE degradation. This result suggests that crystal size may be an important factor to consider in determining the activity of the TiO_2 photocatalyst. Further work in obtaining rutile TiO_2 catalysts with crystal sizes smaller than 40 nm would give more insight into this problem.

CONCLUDING REMARKS

This work has demonstrated that the modified sol–gel method developed in the present study provides a precise control over the primary and secondary particle sizes of TiO_2 catalyst along with their crystalline-phase structure and morphology. Highly reproducible nanometer-sized anatase TiO_2 catalysts as small as 2.3 nm were obtained using a combination of thermal and hydrothermal treatment processes. The N_2 physi-adsorption measurement indicates that the primary particle size dictates the surface area of the TiO_2 catalyst, whereas the aggregate size does not have an effect on the surface area.

Reaction studies conducted using gas-phase photo-oxidation of TCE as a probe reaction show that both the primary and secondary particle sizes of the TiO_2 affect the catalyst activity. The results suggest that in order to properly interpret the reaction data, a careful distinction between the crystal and aggregate sizes must be made. Previous work in photocatalysis usually ignores the effects of TiO_2 aggregation and in some cases there was apparent confusion between the TiO_2 crystal and aggregate sizes. In this study, it

is clear that the aggregate morphology and size control the amount of photons reaching the core of the ensemble.

The TCE degradation over TiO_2 catalyst exhibits a maximum at a primary particle size of 7 nm. For TiO_2 catalysts with primary particle or crystal size larger than 7 nm, the smaller crystals offer a larger surface area and exhibit higher TCE degradation. The subsequent drop in catalyst activity for crystal sizes smaller than 7 nm may be due to changes in the structural and electronic properties of the nanometer crystals. In order to determine their relative contributions, studies should be conducted using structurally sensitive and insensitive reactions to probe the catalyst behavior. In addition, photo-oxidation of organic compounds with different redox properties should also shed more light on catalyst performance.

ACKNOWLEDGMENTS

The authors gratefully acknowledge funding from the Hong Kong Research Grant Councils (grants RGC-HKUST 6118/97P, RGC-HKUST584/94E, and RGC-HKUST 6026/98P). We also thank Dr. K. M. Moulding and Ms. Y. Zhang of the Material Characterization and Preparation Facility at the HKUST for their help in the TEM imaging. We are also grateful to Ms. M. V. Martinez-Huerta for performing the micro-Raman analysis of the TiO_2 catalysts.

REFERENCES

1. Hester, R. E., and Harrison, R. M., "Volatile Organic Compounds in the Atmosphere." Royal Chem. Soc. London, 1995.
2. Shah, J. J., and Singh, H. B., *Environ. Sci. Technol.* **22**, 1381 (1988).
3. Dibble, L. A., and Raupp, G. B., *Catal. Lett.* **4**, 345 (1990).
4. Hoffmann, M. R., Martin, S. T., Choi, W., and Bahnemann, D. W., *Chem. Rev.* **95**, 69 (1995).
5. Mills, A., Davies, R. H., and Worsley, D., *Chem. Soc. Rev.*, 417 (1993).
6. Fox, M. A., and Dulay, T., *Chem. Rev.* **93**, 341 (1993).
7. Peral, J., and Ollis, D. F., *J. Catal.* **136**, 554 (1992).
8. Sauer, M. L., and Ollis, D. F., *J. Catal.* **158**, 570 (1996).
9. Larson, S. A., Widegren, J. A., and Falconer, J. L., *J. Catal.* **157**, 611 (1998).
10. Fu, X., Teltner, W. A., Anderson, M. A., *Appl. Catal. B: Environ.* **6**, 209 (1995).
11. Nimlos, M. R., Jacoby, W. A., Blake, D. M., and Milne, T. A., *Environ. Sci. Technol.* **27**, 732 (1993).
12. Muggli, D. S., Larson, S. A., and Falconer, J. L., *J. Phys. Chem.* **100**, 15886 (1996).
13. Maira Vidal A. J., Soria, J., Augugliaro, V., and Loddo, V., *Chem. Biochem. Eng. Q.* **11(2)**, 89 (1997).
14. Djeghri, N., and Teichner, S. J., *J. Catal.* **62**, 99 (1980).
15. Li Puma, G., and Yue, P. L., *Environ. Sci. Technol.* **33**, 3210 (1999).
16. Li Puma, G., and Yue, P. L., *Ind. Eng. Chem. Res.* **38**, 3246 (1999).
17. Brus, L., *J. Phys. Chem.* **90**, 2555 (1986).
18. Kariyone, T., Anpo, M., Chiba, K., and Tomonari, M., *Hyomen (Surface)* **29**, 156 (1991).
19. Martin, C. A., Baltanas, M. A., and Cassano, A. E., *J. Photochem. Photobiol. A: Chem.* 199 (1993).
20. Stamatakis, P., Salzman, G. C., Bohren, C. F., and Allen, T. B, *J. Coatings Technol.* **62**, 95 (1990).
21. Anpo, M., Shima, T., Kodama, S., and Kubokama, Y., *J. Phys. Chem.* **91**, 4305 (1987).
22. Xu, N., Shi, Z., Fan, Y., Dong, J., Shi, J., and Hu, M. Z.-C., *Ind. Eng. Chem. Res.* **38**, 373 (1999).
23. Wang, C.-C., Zhang, Z., and Ying, Y. J., *Nanostr. Mater.* **9**, 583 (1997).
24. Zhang, Z., Wang, C.-C., Zakaria, R., and Ying, Y., *J. Phys. Chem. B* **102**, 10871 (1998).
25. Rivera, P., Tanaka, K., and Hisanaga, T., *Appl. Catal. B: Environ.* **3**, 37 (1993).
26. Dong Jang, H., *AIChE J.* **43**, 2704 (1997).
27. Kobata, A., Kusakabe, K., and Morooka, S., *AIChE J.* **37**, 347 (1991).
28. Akhtar, M. K., Xiong, Y., and Pratsinis, S. E., *AIChE J.* **37**, 1561 (1991).
29. Suyama, Y., Ohmura, K., and Kato, A., *J. Jpn. Chem. Soc.* **59**, 146 (1976).
30. Nishiwaki, K., Kakuta, N., Ueno, A., and Nakabayashi, H., *J. Catal.* **118**, 498 (1989).
31. Nagpal, V. J., Davis, R. M., and Desu, S. B., *J. Mater. Res.* **10**, 3068 (1995).
32. Khalil, K. M. S., and Zaki, M. I., *Powder Technol.* **92**, 233 (1997).
33. Brinker, C. J., and Scherer, G. W., "Sol-gel science: the physics and chemistry of sol-gel processing," Chap 13. Academic Press, New York, 1990.
34. Honch, L. L., and West, J. K., *Chem. Rev. (Washington D.C.)* **90**, 33 (1990).
35. Jean, J. H., and Ring, T. A., *Colloids Surf.* **29**, 273 (1988).
36. Terabe, K., Kato, K., Miyazaki, H., Yamaguchi, S., and Imai, A., *J. Mater. Sci.* **29**, 1617 (1994).
37. Yoldas, B. E., *J. Mater. Sci.* **21**, 1087 (1986).
38. Sarai, H., Kawahara, H., Shimazaki, M., and Abe, M., *Langmuir* **14**, 2208 (1998).
39. Clark, H. B., *Aerosol Sci. Technol.* **23**, 553 (1995).
40. Xia, B., Huang, H., and Xie, Y., *Mater. Sci. Eng. B* **57**, 150 (1999).
41. Barrer, R. J., "Hydrothermal Chemistry of Zeolites." Academic Press, New York, 1982.
42. Hirano, M., and Kato, E., *J. Am. Ceram. Soc.* **82(3)**, 786 (1999).
43. Rohlkuhn, B., Wittmann, R., Meyer, K., and Schultze, D., *Mikrochim. Acta* **125**, 21 (1997).
44. Guinier, A., "X-ray Diffraction in Crystals, Imperfect Crystals, and Amorphous Bodies," p. 121. Dover, New York, 1994.
45. Iida, Y., Furukawa, M., Aoki, T., and Sakai, T., *Appl. Spectrosc.* **52**, 673 (1998).
46. Zhang, Y.-H., Chan, C. K., Porter, J. F., and Guo, W., *J. Mater.* **9**, 2602 (1998).
47. Siegel, R., and Howell, J. R., "Thermal Radiation Heat Transfer." Hemisphere, Washington, DC, 1992.
48. Van de Hulst, H. C., "Light Scattering by Small Particles." Dover, London, 1981.
49. Bacsa, R. R., and Kiwi, J., *Appl. Catal. B: Environ.* **16**, 19 (1998).
50. Bickley, R. I., Gonzalez-Carreno T., Lees J. S., Palmisano, L., and Tilley, R. J. D., *J. Solid State Chem.* **92**, 178 (1991).
51. Zhao, J., Wang Z., Wang L., Yang, H., and Zhao M., *J. Mater. Sci Lett.* **17**, 1867 (1998).